

Article

Open Access



# ZnO/MgZnO heterostructure membrane with type II band alignment for ceramic fuel cells

M.A.K. Yousaf Shah<sup>1</sup> , Yuzheng Lu<sup>2,\*</sup>, Naveed Mushtaq<sup>1</sup>, Manish Singh<sup>3</sup>, Sajid Rauf<sup>4</sup>, Muhammad Yousaf<sup>1</sup>, Bin Zhu<sup>1,\*</sup>

<sup>1</sup>Jiangsu Provincial Key Laboratory of Solar Energy Science and Technology/Energy Storage joint Research Center, School of Energy and Environment, Southeast University, Nanjing 210096, Jiangsu, China.

<sup>2</sup>School of Electronic Engineering, Nanjing Xiao Zhuang University, Nanjing 211171, Jiangsu, China.

<sup>3</sup>School of Materials Science and Engineering, Helmerich Research Center, Oklahoma State University, Tulsa, OK 74106, USA.

<sup>4</sup>College of Electronics and Information Engineering, Shenzhen University, Shenzhen 518000, Guangdong, China.

\***Correspondence to:** Prof. Bin Zhu, Jiangsu Provincial Key Laboratory of Solar Energy Science and Technology/Energy Storage joint Research Center, School of Energy and Environment, Southeast University, No.2 Si Pai Lou, Nanjing 210096, Jiangsu, China. E-mail: zhu-bin@seu.edu.cn; Dr. Yuzheng Lu, School of Electronic Engineering, Nanjing Xiao Zhuang University, Nanjing 211171, Jiangsu, China. E-mail: mrluyuzheng@163.com

**How to cite this article:** Shah MAKY, Lu Y, Mushtaq N, Singh M, Rauf S, Yousaf M, Zhu B. ZnO/MgZnO heterostructure membrane with type II band alignment for ceramic fuel cells. *Energy Mater* 2022;2:200031. <https://dx.doi.org/10.20517/energymater.2022.27>

**Received:** 13 May 2022 **First Decision:** 9 Jun 2022 **Revised:** 25 Jul 2022 **Accepted:** 10 Aug 2022 **Published:** 25 Aug 2022

**Academic Editors:** Yuping Wu, Yuhui Chen **Copy Editor:** Tiantian Shi **Production Editor:** Tiantian Shi

## Abstract

Semiconductor membrane fuel cells are a new promising R&D for solid oxide fuel cells and proton ceramic fuel cells. There is a challenge of the electronic short circuit issue by using semiconductor to replace conventional electrolyte membrane. In this work, type II band alignment of the semiconductor heterostructure based on Mg-doped ZnO and ZnO can, on one hand, block electrons passing through the junction, and on the other hand, trigger the ionic properties of membrane to boost the fuel cell performance. The Mg doping into ZnO creates more oxygen vacancies at the surface of ZnO, leading to enhanced ionic transport, and meaningful fuel cell performance of 673 mW/cm<sup>2</sup>; while the Mg-doped ZnO/ZnO heterostructure fuel cell has delivered 997 mW/cm<sup>2</sup> and OCV 1.04 V at 520 °C. It is worth highlighting that the constructed heterostructure interface, especially the band bending and constituted build-in electric field, plays a pivotal role in enhancing the ionic transport and suppressing the electron passing through the internal device. First principal calculations using density functional theory confirmed the doping of Mg and the formation of heterostructure with ZnO to help for enhancing charge carriers and separations. This work suggests that the constructed type II band alignment or the semiconductor heterostructure is useful for developing advanced fuel cells.



© The Author(s) 2022. **Open Access** This article is licensed under a Creative Commons Attribution 4.0 International License (<https://creativecommons.org/licenses/by/4.0/>), which permits unrestricted use, sharing, adaptation, distribution and reproduction in any medium or format, for any purpose, even commercially, as long as you give appropriate credit to the original author(s) and the source, provide a link to the Creative Commons license, and indicate if changes were made.



**Keywords:** Type-II semiconductor heterostructure, ZnO/Mg-ZnO, ceramic fuel cells, high ionic conductivity

## INTRODUCTION

Advanced ceramic fuel cells, e.g., solid oxide fuel cells (SOFCs) and proton ceramic fuel cells (PCFCs), have an emerging need for the discovery of new functional materials that can exhibit more advanced electrolyte functions at low temperature (< 600 °C). Semiconductor oxides have opened a new path to fulfilling this strategy. In particular, the physical and electrical properties of ZnO make it the most suitable and alternative candidate for fuel cell technology. Among all semiconductors, ZnO, with a broad energy bandgap (3.1 eV), is regarded as one of the most promising semiconductors in all fields of science, especially in fuel cells, due to its excellent power density and ionic conductivity<sup>[1-3]</sup>. It is well known that the doping of semiconductors into the host element can change the energy bandgap, which primarily influences the device performance. On this basis, Xia *et al.* proposed that the doping of Li into ZnO causes a reduction in the energy bandgap, leading to enhanced fuel cell performance and better ionic conductivity<sup>[4]</sup>. Furthermore, many semiconductors have been reported to tune the energy bandgap using the doping or coating approach to improve the ionic conductivity of fuel cell devices<sup>[5-10]</sup>. Recently, the semiconductor heterostructure (SH) approach has become the most popular method and is regarded as the key to enhancing ionic conductivity without short-circuiting. The distribution and movement of charge carriers in a SH are mainly dependent on the potential barrier height at the interface, which can be experienced by electrons and holes at the heterostructure of the semiconductor. The band offset of the conduction bands (CBs) and valence bands (VBs) is created due to band bending at the interface, giving rise to the measurement of the potential barrier at the heterostructure interface<sup>[11-15]</sup>.

According to energy band alignment, there are two leading types of semiconductor heterostructures, namely, type I and type II. In type-I SHs, both electrons and holes experience the potential barrier, which is in contrast to type-II SHs, where the potential barrier can be experienced using either electrons or holes. Furthermore, in type-I SH, the bandgap of semiconductor (1) is lower than semiconductor (2) and the CB of semiconductor (2) is at a higher position than semiconductor (1), while the potential of the VB of semiconductor (2) is at a lower position than for semiconductor (1). Electrons can be transferred from semiconductor (1) to semiconductor (2), leading to the accumulation of the charge carriers in semiconductor (2). The accumulation of charge carriers facilitates the charge recombination and decreases the electron mobility and activity. In type-II SH semiconductor (2), the CB is more negative compared to semiconductor (1) and the VB of semiconductor (1) is more positive in comparison to semiconductor (2). This scheme enables the flow of electrons and holes in the reverse direction, leading to the migration of electrons from semiconductor (2) to semiconductor (1) and holes from semiconductor (1) to semiconductor (2). Type-II SHs suppress the electronic conduction, as reported elsewhere<sup>[1]</sup>. Both type-I and type-II SHs are the most suitable for designing energy conversion and storage devices, as they suppress the electronic conduction to prevent the device from short-circuiting<sup>[16-21]</sup>. Among them, type-II SH exhibiting a large exciton binding energy (ZnO 60 meV, MgO 80 meV), wide tunable band gap, and either of the charge carrier types (electrons or holes) experiences the potential barrier at the heterojunction. By taking these advantages of type-II SH semiconductor, it was used as a membrane to replace the conventional electrolyte for an advanced ceramic fuel cell in this work.

Xia *et al.* proposed a new study using a triple-conducting oxide perovskite  $\text{BaCo}_{0.8}\text{Fe}_{0.8}\text{Zr}_{0.1}\text{Y}_{0.1}\text{O}_3$  electrode composited with ZnO to develop a SH electrolyte, which can enhance the fuel cell performance and high ionic conductivity at 550 °C. The authors proposed an SH approach to improve the fuel cell performance and suppress the electronic conduction using the band alignment mechanism and built-in electric field

(BIEF) at the interface<sup>[1]</sup>. In addition, Shah *et al.* reported a new semiconductor heterostructure based on SrFe<sub>0.2</sub>TiO<sub>3</sub> and ZnO as an electrolyte for fuel cell devices. The proposed semiconductor heterostructure of SrFe<sub>0.2</sub>TiO<sub>3</sub>-ZnO exhibited a peak power density of 650 mW/cm<sup>2</sup>, a high ionic conductivity of 0.21 S cm<sup>-1</sup> and a good open-circuit voltage (OCV) of 1.06 V at 520 °C. The promoted ionic transport and suppression of electronic conduction were attributed to the developed SH<sup>[22]</sup>. Moreover, new semiconductors with the multifunctional properties of cubic silicon carbide (3-SiC) were used to establish SHs by introducing the n-type semiconductor ZnO. The prepared heterostructure of (n-n)3-SiC-ZnO delivered an enhanced ionic conductivity of 0.12 S.cm<sup>-1</sup> with a fuel cell performance of 270 mW/cm<sup>2</sup> at 550 °C. The BIEF and energy band alignment of heterostructure semiconductors play a significant role in superficial ionic transport and the suppression of electronic conductivity<sup>[15]</sup>. In addition, more studies have been published using the SH approach to boost fuel cell performance and high ionic conductivity<sup>[11-15]</sup>. As mentioned earlier, it is noteworthy that all the reports are well matched with the type-II heterostructure. Researchers have used ZnO/Mg-ZnO SH approaches to enhance device performance by tuning the energy bandgap, especially in the optoelectronics field, but not for fuel cells<sup>[20,21]</sup>.

Analyzing the benefits of the SH approach and the multifunctional properties of ZnO, we first develop a Mg-ZnO semiconductor by a suitable doping approach. Furthermore, we construct a ZnO/Mg-ZnO heterostructure using energy band alignment. The co-precipitation approach is applied to prepare the ZnO and Mg-ZnO, and the solid blending technique is then used to develop the ZnO/Mg-ZnO SH. The type-II SH approach enhances the ionic transport and suppresses the electronic carriers at the interface using band bending and the BIEF. These results highlight that the prepared type-II ZnO/Mg-ZnO SH may significantly benefit fuel cell technology.

## EXPERIMENTAL SECTION

### Material preparation

ZnO was prepared using a co-precipitation technique. In detail, a certain amount of Zn(NO<sub>3</sub>)<sub>2</sub> was dissolved in 500 mL of deionized water and placed for mixing on a stirrer to form a 0.5 mol L<sup>-1</sup> solution. Meanwhile, Na<sub>2</sub>CO<sub>3</sub> was dissolved in 200 mL of deionized water in another beaker and set for stirring to form a 1 mol L<sup>-1</sup> solution. Next, the precipitant agent Na<sub>2</sub>CO<sub>3</sub> was poured dropwise into the solution of Zn(NO<sub>3</sub>)<sub>2</sub> to form the precipitates of the prepared solution. The molar ratio of Zn(NO<sub>3</sub>)<sub>2</sub> and Na<sub>2</sub>CO<sub>3</sub> was 1:2 in the given solution. After precipitation, the solution was filtered using suction pump-supported filter paper and then washed with ethanol and deionized water three times to remove the surface impurities, followed by drying at 120 °C for 24 h and sintering at 600 °C for 3 h in the open air. Zn<sub>0.8</sub>Mg<sub>0.2</sub>O was prepared using Mg(NO<sub>3</sub>)<sub>2</sub> and Zn(NO<sub>3</sub>)<sub>2</sub> with the appropriate amount of Na<sub>2</sub>CO<sub>3</sub> following the above procedure. The molar ratio between the nitrates and the precipitating agent was 1:2. Finally, the ZnO/Mg-ZnO composite was prepared using ZnO and Zn<sub>0.8</sub>Mg<sub>0.2</sub>O powders with a 1:1 (w/w) ratio by a blending method. Other ratios of doping (Zn<sub>0.7</sub>Mg<sub>0.3</sub>O and Zn<sub>0.9</sub>Mg<sub>0.1</sub>O) and different groups of heterostructures (1:2 and 2:1) were also prepared to test the fuel cell performance.

### Fuel cell fabrication

The prepared powder of ZnO, Mg-ZnO and ZnO/Mg-ZnO was used as an electrolyte, while the NCAL-Ni made of Ni foams painted with Ni<sub>0.8</sub>Co<sub>0.15</sub>Al<sub>0.05</sub>Li-oxide was used as a symmetrical electrode. The NCAL electrode was made by pasting the slurry of NCAL (made by mixing commercial NCAL powder with an appropriate amount of terpinol) and then placing it for heating at 120 °C for 30 min to dry the electrodes. The three-pellet fuel cell device was prepared by compacting the electrolytes (ZnO, Mg-ZnO and ZnO/Mg-ZnO) among the two symmetrical electrodes uniaxially under an applied pressure load of 200 MPa to obtain a pellet (Ni-NCAL/electrolyte/NCAL-Ni) with a 13-mm diameter and a 1.5-mm thickness, along with an active area of 0.64 cm<sup>2</sup>.

## Characterization

X-ray diffraction (XRD) was performed to investigate the phases of ZnO, Mg-ZnO and ZnO/Mg-ZnO using a Bruker D8 X-ray diffractometer with Cu K $\alpha$  radiation from 20° to 80° at the rate of 10° min<sup>-1</sup>. Transmission electron microscopy (TEM) supported by EDX and field-emission scanning electron microscopy [FESEM, JSM7100F (JEOL)] was performed to evaluate the morphologies of the samples. Using UV-visible spectroscopy and ultra-photoelectron spectroscopy (UPS), the energy bandgap and VB maximum position were determined. X-ray photoelectron spectroscopy (XPS) was performed to investigate the surface properties of the prepared samples.

## Electrochemical measurements

Impedance spectroscopy (EIS) measurements were taken using a Zennium-E (ZAHNER, Germany) at a frequency range of 0.1-10<sup>6</sup> Hz. To obtain the performance of the cells, a fuel cell tester (ITECH DC ELECTRONIC LOAD, IT8511) was used to record the temperatures ranging from 550 to 490 °C. The flow rate of hydrogen and oxygen was 100 mL min<sup>-1</sup>. A fuel cell durability test was performed with a constant current density of 110 mA/cm<sup>2</sup> at 520 °C under an H<sub>2</sub>/air environment.

## Simulation and numerical analysis

The density of states (DOS) and structural optimization were performed using the DFT framework as implemented in the Atomistic Toolkit (ATK) with the generalized gradient approximation (GGA). Instead of employing the local density approximation (LDA), we preferred the GGA exchange-correlation functional for the relative DOS properties of ZnO, Mg-ZnO and ZnO/Mg-ZnO. The GGA scheme is also better for physically adding vacancies at the surface or doping in the inner or center. Using the Virtual NanoLab Software, GGA was coupled with a non-equilibrium green function for calculating the energy band structure of the materials and the DOS for possible fuel cell applications. To accomplish the task, we selected Mg, Zn and O from the software database to set up its cleavage surface to be oriented along the Y-Z plane of ZnO, Mg-ZnO and ZnO/Mg-ZnO. For the first set of calculations, the k-point sampling was selected to be 5 × 5 × 100 with the GGA exchange-correlation potential. From the numerical analysis, the grid mesh cut-off of 125 Ha with the Fermi-Dirac occupation method was chosen to perform the DOS calculation and structural optimization. We optimized and achieved the DOS calculation by employing a force tolerance of 0.05 eV/Å.

## RESULTS AND DISCUSSION

### Crystalline structure and morphological analysis

Figure 1A and B show the original and magnified XRD patterns of ZnO, Mg-ZnO and ZnO/Mg-ZnO. The peaks correspond to the (100), (002), (101), (102), (110), (103) and (112) planes. The sharp diffraction peaks signify the well-crystallized structures of ZnO, Mg-ZnO and ZnO/Mg-ZnO. The obtained XRD patterns show no sign of MgO or any other impurities signifying that Mg<sup>2+</sup> was successfully doped into ZnO in the form of pure wurtzite hexagonal structure. Furthermore, neither a peak shift nor any difference in the phase was found in the composite phase, indicating the formation of the ZnO/Mg-ZnO composite heterostructure<sup>[21,22]</sup>. No extra peaks were observed, eliminating the possibility of any reaction between the composite materials. According to the Debye-Scherrer equation, the calculated crystalline size for ZnO is 26 nm, while for Mg-ZnO, this value is 24 nm, which might be due to the doping of Mg into the ZnO lattice. Moreover, due to the doping effect, peak shifting was noticed because of the different radii of Mg<sup>2+</sup> (0.57 Å) and Zn (0.60 Å) following Vegard's law<sup>[10]</sup>. The XRD analysis of the synthesized heterojunction after the fuel cell measurements was also evaluated, as displayed in Supplementary Figure 1.

Figure 1C displays the HR-TEM images for the morphological confirmation of the ZnO/Mg-ZnO composite heterostructure. The image shows that Mg-ZnO is well incorporated with ZnO in the shape of

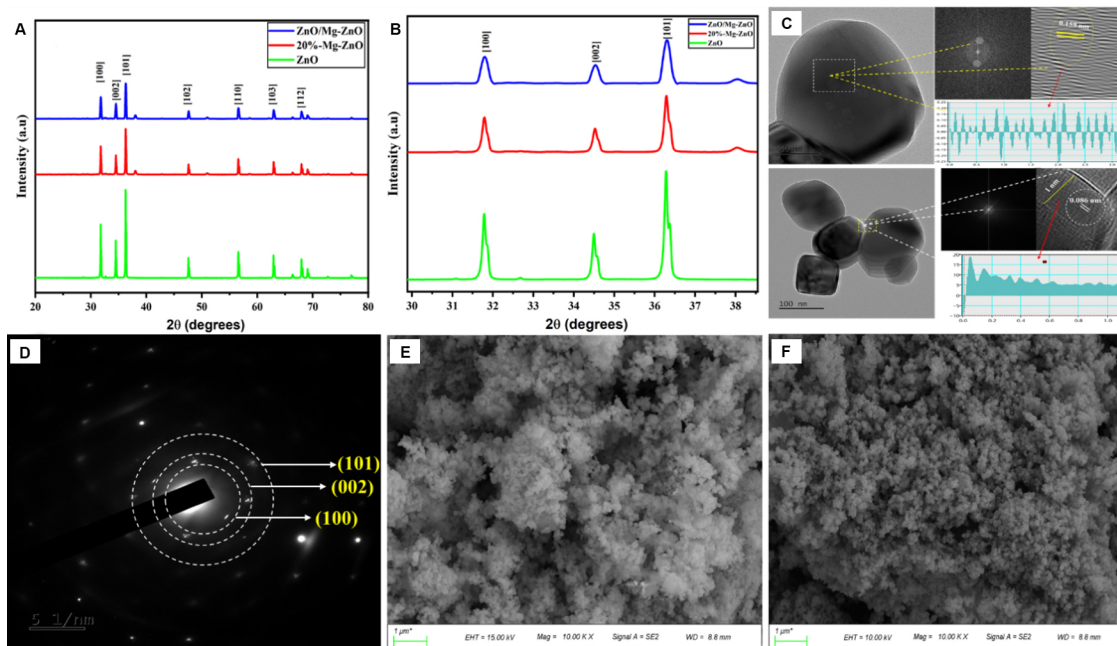


**Figure 1.** (A) Original and (B) magnified XRD patterns of ZnO, Mg-ZnO and ZnO/Mg-ZnO. (C) HR-TEM images of ZnO/Mg-ZnO composite SH with (D) lattice plane and SAED pattern of diffraction planes. SEM images of (E) ZnO and (F) ZnO/Mg-ZnO. SAED: Selected area of electron diffraction.

the core-shell heterostructure. The interplanar *d* spacings for the composite SH are 0.159 and 0.087 nm, corresponding to ZnO and Mg-ZnO, respectively, which are well matched with the XRD analysis. Essentially, the particles are on the nanoscale, which is advantageous for better results. Furthermore, the lack of impurity phases guarantees the successful formation of the SH with multiple active sites, leading to enhanced ionic transport. The particles are crosslinked, manifesting the facile and fast transport of charge carriers through the interface<sup>[11–15]</sup>. **Figure 1D** reveals the selected area of electron diffraction (SAED) pattern of ZnO/Mg-ZnO with bright spots (diffraction rings) due to electron diffraction. Each spot is instigated via a set of parallel planes within the synthesized crystal structure, influencing the diffraction condition. Miller indices were allotted accordingly and the pattern is indexed with different planes of (002), (100) and (101), which are well matched with the hexagonal structure, as displayed in **Figure 1D**<sup>[21]</sup>. The SEM images of ZnO and ZnO/Mg-ZnO reveal a morphology with an irregular and uniform distribution of particles, leading to a perfect connection. As exhibited in **Figure 1E** and **F**, they enable easy and fast transport. **Supplementary Figure 2A–F** show the HRTEM-EDS of ZnO/Mg-ZnO, revealing a uniform distribution for all elements in the prepared composite.

### Fuel cell performance

The electrochemical fuel cell performance of the ZnO, Mg-ZnO and ZnO/Mg-ZnO electrolytes was determined to measure the *I*-*V* (current-voltage) and *I*-*P* (current-power density) characteristics under an H<sub>2</sub>/air environment at 420–520 °C. Due to the exceptionally low ionic conductivity of pure ZnO, the electrochemical performance of ZnO is 459 mW cm<sup>-2</sup>, which is not sufficient to realize its functionality as an efficient electrolyte. Such a performance of ZnO might be due to the injection of protons and oxide ions, which leads to activation of the device and enhanced fuel cell performance. In addition, thermally activated ions with increasing temperature mainly enhanced the performance of ZnO and the corresponding materials<sup>[1]</sup>. The doping approach was proven to enhance the ionic conductivity and fuel cell performance with a power output of 673 mW cm<sup>-2</sup> at 520 °C. Furthermore, to further improve the performance to a

higher level, the hybrid ZnO/Mg-ZnO heterostructure was developed to achieve a higher fuel cell performance of  $997 \text{ mW cm}^{-2}$  at  $520 \text{ }^\circ\text{C}$ , which is approximately double that of the pure ZnO electrolyte. The fuel cell performance of ZnO, Mg-ZnO and ZnO/Mg-ZnO can be revealed in [Figure 2A-C](#) at  $420\text{-}520 \text{ }^\circ\text{C}$ . The higher OCV and better fuel cell performance signify the prevention of short-circuiting in the fuel cell devices. In addition, the significantly higher performance results from the doping and heterostructure formation, especially the band alignment and BIEF at the interface<sup>[1,12,13,15]</sup>. The obtained fuel cell performance is higher than those in the reported literature, illustrating that the prepared SH holds excellent potential for fuel cell technology<sup>[1,12,14,15,20]</sup>.

Moreover, symmetrical electrodes (anode and cathode) NCAL with better catalytic activity were used, significantly contributing to the enhanced fuel cell performance, as reported previously<sup>[5-15]</sup>. The comparison between the presented electrolytes regarding fuel cell performance at different temperatures is visualized in [Figure 2D](#). Moreover, the fuel cell performance at different doping contents and a composite heterostructure with different ratios was evaluated and is presented in [Supplementary Figure 3A and B](#).

### EIS and XPS analysis

To investigate the ion transfer kinetics of the process, EIS analysis of ZnO, Mg-ZnO and ZnO/Mg-ZnO was carried out under an  $\text{H}_2/\text{air}$  environment at different operating temperatures of  $420\text{-}520 \text{ }^\circ\text{C}$ , as displayed in [Figure 3A-C](#). The EIS curves of Mg-ZnO and ZnO/Mg-ZnO reveal the ionic conduction behavior due to appropriate doping and heterostructure development. These results imply that the doping and development of the composite remarkably enhance the ionic conductivity by incorporating Mg into ZnO and then constructing the ZnO/Mg-ZnO SH. The obtained arcs were divided into three regions, namely, the high-frequency region attributed to the bulk behavior, the intermediate-frequency region related to the grain boundary behavior and the low-frequency region belonging to the electrode behavior. All the arcs will not appear simultaneously due to different relaxation time constants for the individual polarization of conducting materials<sup>[1,4,11,15]</sup>. The GB arcs tend to disappear with increasing temperature, and as a result, a single arc is shown in [Figure 3A-C](#). Furthermore, a similar relaxation time for the grains and grain boundaries might be the reason for such behavior<sup>[5-10]</sup>. Therefore, to distinguish the grain, grain boundary and electrode contributions, the obtained EIS data for all materials were fitted using the  $R_o(R_1Q_1)(R_2Q_2)$  circuit through ZSIMPWIN software. The detailed parameters of the fitted circuit can be found elsewhere<sup>[12]</sup>. The exact values of all parameters are listed in [Supplementary Tables 1-3](#). Lower ohmic and grain boundary resistance values manifest rapid charge transport, leading to enhanced ionic conductivity of Mg-ZnO and ZnO/Mg-ZnO at  $420\text{-}520 \text{ }^\circ\text{C}$ . There is no doubt that low ohmic(grain) and grain boundary resistance values contribute immensely to enhancing the ionic carrier. In addition, the electrode resistance has also exhibited declining behavior in all EIS spectra, as shown in [Figure 3A-C](#), manifesting better catalytic activity of electrodes<sup>[23,24]</sup>.

Using the ohmic polarization region, the polarization curve slope helps infer ionic conductivity ( $\sigma_i$ ). The central region of the  $I\text{-}V$  curve represents the ohmic polarization resistance, which gives the ionic conductivity using  $\sigma_i = L/RA$ . The obtained ionic conductivity falls in the range of  $0.10\text{-}0.03$ ,  $0.135\text{-}0.05$  and  $0.16\text{-}0.08 \text{ S cm}^{-1}$  for ZnO, Mg-ZnO and ZnO/Mg-ZnO at  $420\text{-}520 \text{ }^\circ\text{C}$ , respectively, as shown in [Figure 3D](#). The attained ionic conductivity values for the composite SH are higher than for ZnO and Mg-ZnO<sup>[10,12,15]</sup>. Such reliable ionic conduction is a result of the formation of the SH and constituted BIEF at the interface, which acts as driving forces to enhance the ionic carriers.

The full XPS spectra of all materials are displayed in [Figure 3E](#), revealing the existence of all elements. The XPS peaks of Zn and Mg were identified without any impurity, where both the atoms are in the oxidation

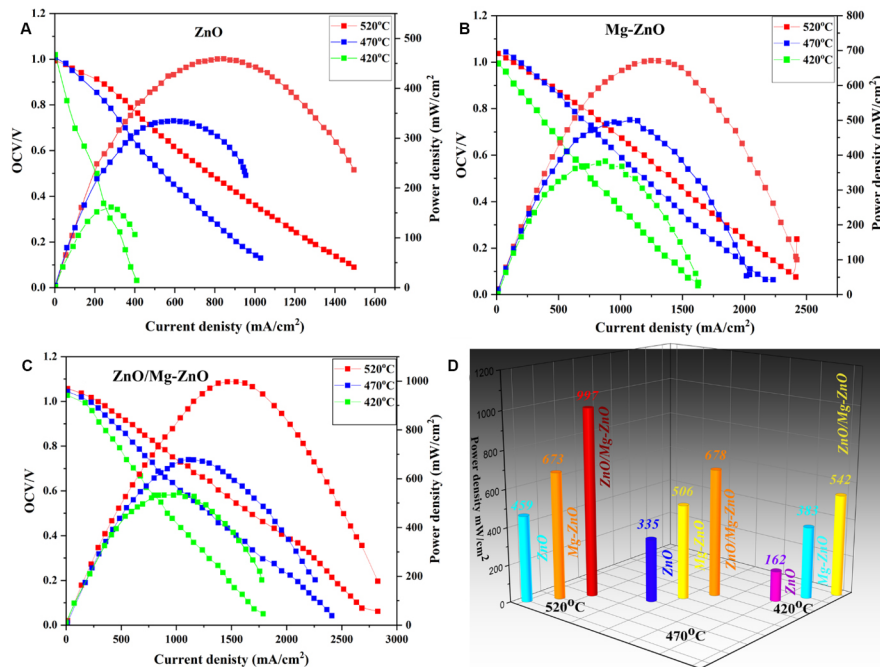


**Figure 2.** Fuel cell performance of (A) ZnO, (B) Mg-ZnO and (C) ZnO/Mg-ZnO at different temperatures (420–520 °C) and (D) comparison between ZnO, Mg-ZnO and ZnO/Mg-ZnO.

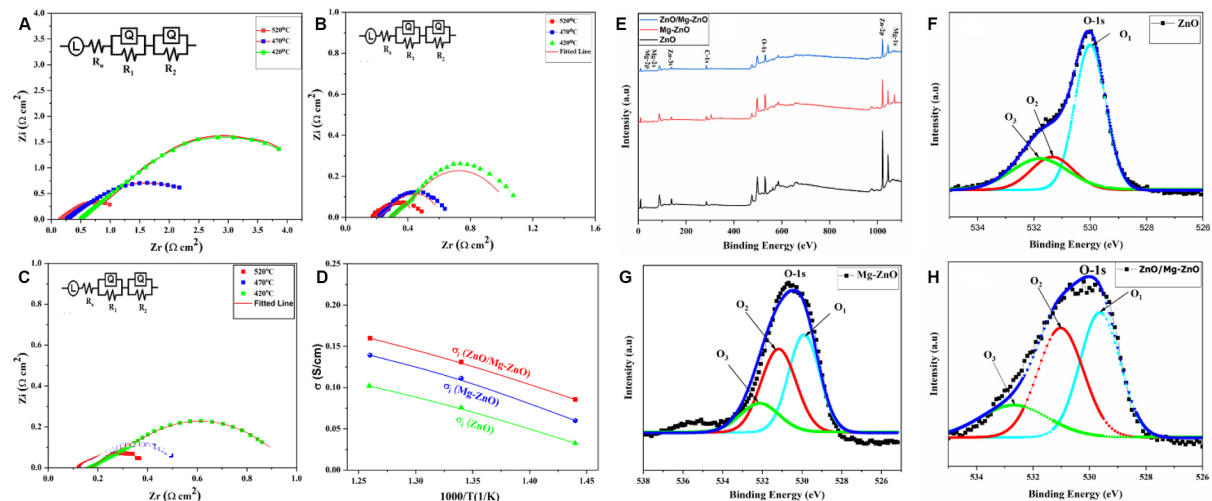


**Figure 3.** EIS spectra of (A) ZnO, (B) Mg-ZnO and (C) ZnO/Mg-ZnO. (D) Ionic conductivity of ZnO, Mg-ZnO and ZnO/Mg-ZnO at 420–520 °C. (E) Full XPS spectra and O 1s spectra of (F) ZnO, (G) Mg-ZnO and (H) ZnO/Mg-ZnO.

state of  $2+$  [25,26]. The O 1s spectra for ZnO, Mg-ZnO and ZnO/Mg-ZnO were fitted into three peaks,  $O_1$ ,  $O_2$  and  $O_3$ , as shown in Figure 3F–H. The peak centered at  $\sim 530$  eV corresponds to the  $O^{2-}$  ions in ZnO, Mg-ZnO and ZnO/Mg-ZnO of the hexagonal structure. The second fitted peak centered around the binding energy of 531.5 eV representing the oxygen vacancies in ZnO, Mg-ZnO and ZnO/Mg-ZnO, while the third fitted peak lies around the binding energy of 532.3 eV, which can be attributed to the hydroxyl species on the surface of the presented lattice [15,27–30]. Mg-ZnO and ZnO/Mg-ZnO have higher intensity and their peak areas are enhanced by more than 50% compared to ZnO, revealing that doping and constructing heterostructure, leading to an improved concentration for oxygen vacancies that gives rise to enhanced

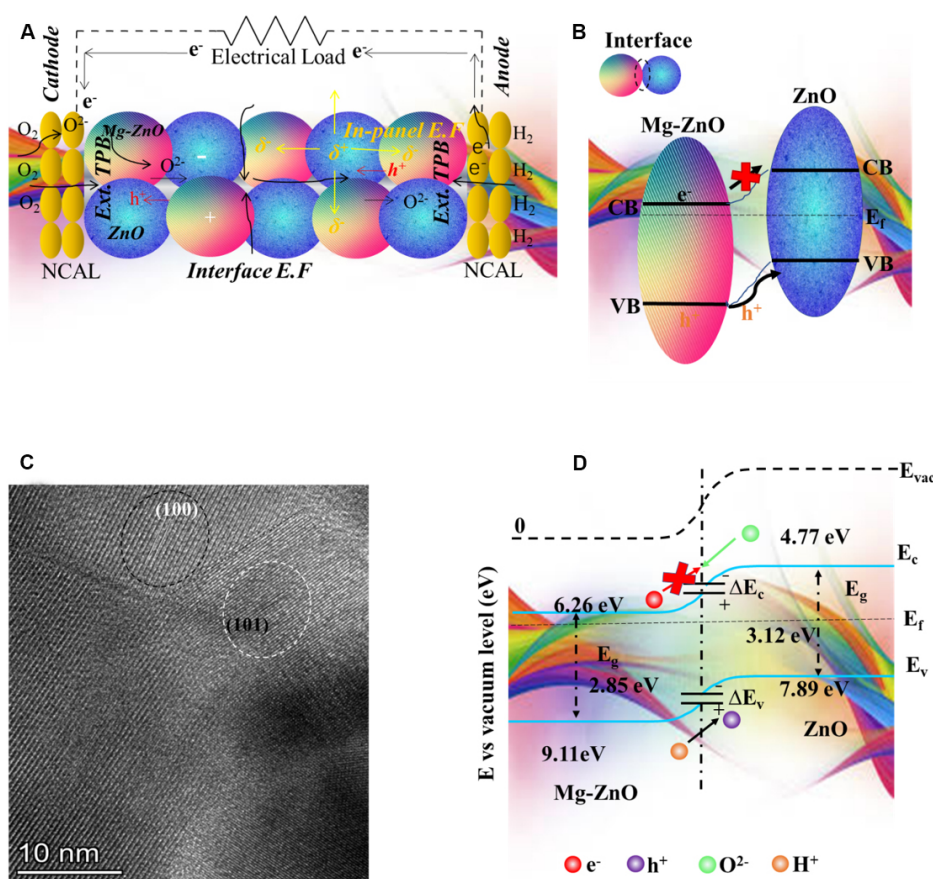


**Figure 4.** (A) Schematic diagram of fuel cell (B-D) diagram of heterojunction along with HR-TEM image of the SH and mechanism of heterojunction.

ionic conductivity<sup>[15]</sup>. In addition, the oxygen vacancies at the surface and interface cause an increase in the charge transport, which boosts the ionic conductivity and performance of the fuel cell device, as reported elsewhere<sup>[31,32]</sup>.

### Type-II energy band alignment phenomena

Based on the obtained results for the  $E_{CB}$ ,  $E_{VB}$  and  $E_g$  [Supplementary Figure 4], the energy band diagrams of ZnO and Mg-ZnO are sketched in Figure 4B and D, respectively. Figure 4A reveals a schematic diagram of constructed fuel cell device. These parameters signify that the SH can be built. On this basis, the electron-blockage mechanism and enhancement in the performance of the type-II SH (ZnO/Mg-ZnO) fuel cell are presented in Figure 4D. In the SH, the charge redistribution appears at the interface constituting the space charge region, producing the BIEF or internal electric field (IEF)<sup>[31-33]</sup>. Furthermore, both materials in the SH have different energies and Fermi levels, and to align the Fermi level, the band bending has been observed, which further causes the VB offset ( $\Delta E_v$ ) and conduction band offset ( $\Delta E_c$ ) to produce the potential barrier. The function of a potential barrier is to inhibit the electronic conduction, the BIEF or IEF, as well as act as a secondary force to suppress the electronic conduction and enhance the ion transport through the SH. In addition, rapid ionic transport has been observed at the grain boundaries between the ZnO/Mg-ZnO SH, and hence the grain boundary behavior is essentially affected by the interface, leading to significantly reduced grain boundary resistance<sup>[1,15]</sup>. The precise formation of the SH is revealed by the HR-TEM images in Figure 4D. The atomic planes of (101) and (111) correspond to ZnO and Mg-ZnO, respectively, revealing the existence of the heterostructure. The HR-TEM image of the heterostructure shows the permeable

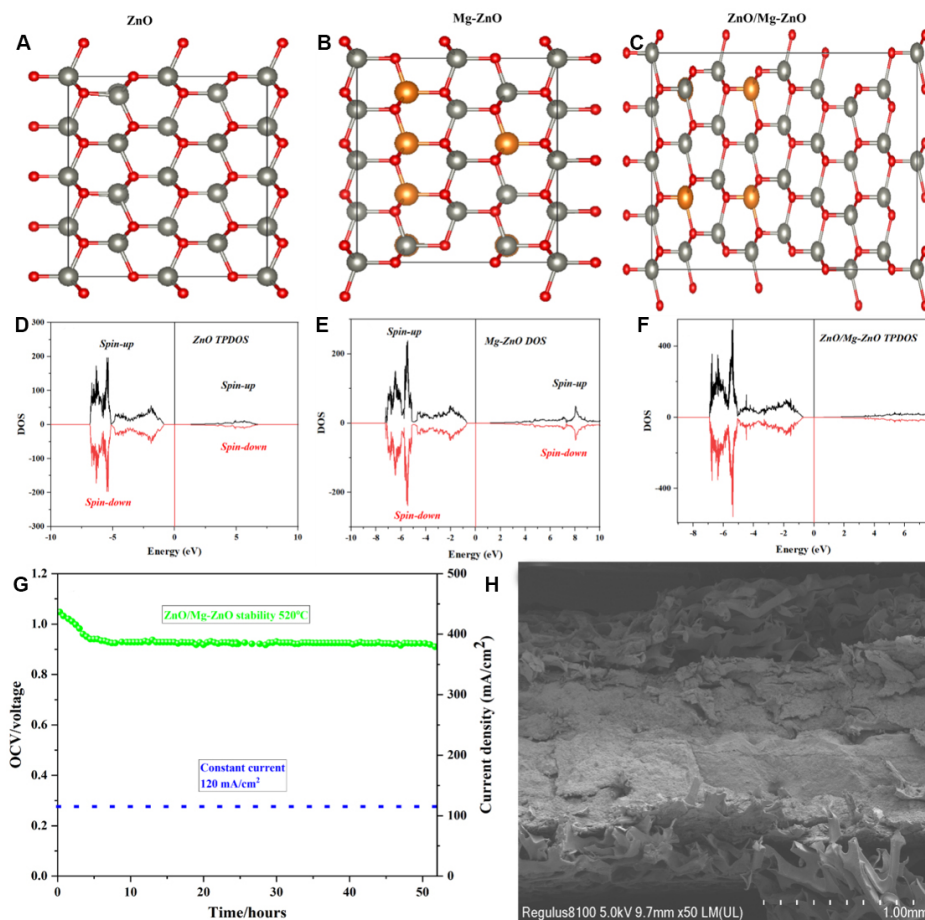


**Figure 5.** Optimized structures of (A) ZnO, (B) Mg-ZnO and (C) ZnO/Mg-ZnO and DOS of (D) ZnO, (E) Mg-ZnO and (F) ZnO/Mg-ZnO. (G) Durability of constructed fuel cell device and (H) cross-sectional view of NCAL/ZnO/Mg-ZnO/NCAL after durability operation.

network to transfer or facilitate the rapid charge transportation of either electrons or ions in Mg-ZnO and ZnO and at the interface of the ZnO/Mg-ZnO SH, as depicted in [Figure 4C](#).

Based on the above results, there are three main reasons to achieve high performance and ionic conductivity and low activation energy. The first reason is to have many active sites to produce more reactions and paths for charge transportation, resulting from the expanded surface area by incorporating Mg into ZnO and decorating the ZnO/Mg-ZnO SH<sup>[1,4,15,32,33]</sup>. The second reason is that the reduced energy bandgap of Mg-ZnO causes the Fermi level to move near the CB so that charges can transport easily and quickly. The final reason is the SH construction, which boosts the ionic conductivity and fuel cell performance using the interfacial properties, as shown in [Figure 4A-D](#).

### DFT calculations and durability analysis

Theoretical calculations were performed using DFT to understand the charge transfer mechanism and to gain further insights into the electrical properties of Mg-ZnO and ZnO/Mg-ZnO, as displayed in [Figure 5A-F](#)<sup>[27,28]</sup>. The structure and the DOS were constructed and studied using Quantum ATK software with the LDA and GGA<sup>[27]</sup>. The PDOS result indicates that the incorporation of Mg into the ZnO lattice causes the creation of additional states with minor defects, which probably points to the existence of oxygen vacancies; however, the overall structure remains in its original state, as shown in [Figure 5E](#)<sup>[34,35]</sup>.

Moreover, the incorporation of Mg into ZnO generates additional DOS, which tends to the bands near the Fermi level, resulting in enhanced charge carrier migration among the CB and VB<sup>[36,37]</sup>. Furthermore, the DOS result is well matched with the experimental result, which shows the reduction of the energy bandgap due to Mg doping in ZnO. In addition, the SH was constructed and optimized with the above-stated parameter (experimental section), as shown in Figure 5C and F. The M-O distances of the constructed heterostructure before and after optimization highlight a different disorder in the structure and all elements, especially oxygen<sup>[34,38,39]</sup>. This displacement and disorder in oxygen in the heterostructure enhance the charge carriers at the interface, improving the ionic conduction, as speculated elsewhere<sup>[34-39]</sup>. Thus, enhanced DOS in the SH near the Fermi level and BIEF at the interface can be interpreted as the valid reason to boost the transfer rate of charge carriers.

To further investigate the reliability of this study and its bearing on fuel cell technology, the durability of ZnO/Mg-ZnO SOFCs was assessed at a low operating temperature of 520 °C. The currently achieved results show that the cells can be subjected to 50 h stable operation at a stationary current density (120 mA cm<sup>-2</sup>) in H<sub>2</sub>/air circumstances, with a constant working voltage of 0.95 V retained for the duration of 50 h [Figure 5G]. A drop in the first few hours in the cell voltage is noticed, which might be due to the activation of electrodes. After 3 h, the cell stays stable for 50 h, as shown in Figure 5G. The cross-sectional view after stability operation is exhibited in Figure 5H. For longer-term durability (> 200 h), more compatible electrode materials and extensive engineering efforts are required and will be the subject of our follow-up work towards this technology.

## CONCLUSION

We have constructed a type-II ZnO/Mg-ZnO semiconductor heterostructure, different from conventional electrolytes used in SOFCs and PCFCs. Mg was doped into ZnO creating more oxygen vacancies at the surface of ZnO and resulting in high ionic conductivity. Furthermore, Mg-ZnO was used to construct the type-II heterostructure with ZnO to deliver impressive ionic conductivity of 0.16 S cm<sup>-1</sup> and high fuel cell performance of 997 mW cm<sup>-2</sup> along with a high OCV (1.01 V) at a low operating temperature of 520 °C. The doping and construction of the ZnO/Mg-ZnO semiconductor heterostructure play crucial roles in promoting the ionic conductivity while suppressing the electronic conduction to avoid the device from short-circuiting.

In addition, semiconductor heterostructure formation has been considered a decisive factor in achieving excellent cell performance. Our observation manifest that facilitated fuel cell performance and high ionic conductivity in the heterostructure is due to rearrangement or reconstruction of atoms and producing the BIEF at the Mg-ZnO/ZnO interface. The band bending/alignment effect is responsible for higher OCV, effectively excluding the risk of short-circuiting. DFT calculations confirmed that doping and construction of heterostructure energy bands move near the Fermi level, which might benefit more charge transportation. Based on the physical mechanism, a new effective strategy should be adopted to develop advanced SH materials for LT-SOFCs and PCFCs. Still, the detailed mechanism and deep understanding of ionic transport and BIEF effect at the interface are yet to be resolved, which can be investigated in further studies.

## DECLARATION

### Authors' contributions

Writing: Shah MAKY, Lu Z, Mushtaq N, Singh M, Rauf S, Yousaf M, Zhu B

Review and Editing: Zhu B, Lu Z

Experimentation: Shah MAKY

Materials characterization: Shah MAKY, Lu Z, Mushtaq N, Singh M, Rauf S, Yousaf M

Data analysis: Shah MAKY, Lu Z, Mushtaq N, Zhu B, Singh M

Conceptualization and methodology: Shah MAKY, Zhu B

### Availability of data and materials

Not applicable.

### Financial support and sponsorship

This work was supported by Southeast University (SEU) PROJET # 3203002003A1 and the National Natural Science Foundation of China (NSFC) under grants # 51772080 and 11604088. Jiangsu Provincial Innovation and Entrepreneurship Talent Program Project No. JSSCRC2021491.

### Conflicts of interest

All authors declared that there are no conflicts of interest.

### Ethical approval and consent to participate

Not applicable.

### Consent for publication

Not applicable.

### Copyright

© The Author(s) 2022.

## REFERENCES

1. Xia C, Mi Y, Wang B, Lin B, Chen G, Zhu B. Shaping triple-conducting semiconductor  $\text{BaCo}_{0.4}\text{Fe}_{0.4}\text{Zr}_{0.1}\text{Y}_{0.1}\text{O}_{3-\delta}$  into an electrolyte for low-temperature solid oxide fuel cells. *Nat Commun* 2019;10:1707. DOI PubMed PMC
2. Lee KM, Lai CW, Ngai KS, Juan JC. Recent developments of zinc oxide based photocatalyst in water treatment technology: a review. *Water Res* 2016;88:428-48. DOI PubMed
3. D'agostino D, Di Giorgio C, Bobba F, et al. Effects of cobalt substitution on ZnO surface reactivity and electronic structure. *J Mater Chem C* 2019;7:8364-73. DOI
4. Xia C, Qiao Z, Shen L, et al. Semiconductor electrolyte for low-operating-temperature solid oxide fuel cell: Li-doped ZnO. *Int J Hydrog Energy* 2018;43:12825-34. DOI
5. Shah MY, Rauf S, Mushtaq N, et al. Semiconductor Fe-doped  $\text{SrTiO}_{3-\delta}$  perovskite electrolyte for low-temperature solid oxide fuel cell (LT-SOFC) operating below 520 °C. *Int J Hydrog Energy* 2020;45:14470-9. DOI
6. Shah MAKY, Zhu B, Rauf S, et al. Electrochemical properties of a Co-doped  $\text{SrSnO}_{3-\delta}$ -based semiconductor as an electrolyte for solid oxide fuel cells. *ACS Appl Energy Mater* 2020;3:6323-33. DOI
7. Shah MAKY, Rauf S, Zhu B, et al. Semiconductor Nb-doped  $\text{SrTiO}_{3-\delta}$  perovskite electrolyte for a ceramic fuel cell. *ACS Appl Energy Mater* 2021;4:365-75. DOI
8. Shah MAKY, Rauf S, Mushtaq N, et al. Novel perovskite semiconductor based on Co/Fe-codoped LBZY ( $\text{La}_{0.5}\text{Ba}_{0.5}\text{Co}_{0.2}\text{Fe}_{0.2}\text{Zr}_{0.3}\text{Y}_{0.3}\text{O}_{3-\delta}$ ) as an electrolyte in ceramic fuel cells. *ACS Appl Energy Mater* 2021;4:5798-808. DOI
9. Rauf S, Zhu B, Shah MY, et al. Tailoring triple charge conduction in  $\text{BaCo}_{0.2}\text{Fe}_{0.1}\text{Ce}_{0.2}\text{Tm}_{0.1}\text{Zr}_{0.3}\text{Y}_{0.1}\text{O}_{3-\delta}$  semiconductor electrolyte for boosting solid oxide fuel cell performance. *Renew Energy* 2021;172:336-49. DOI
10. Mushtaq N, Lu Y, Xia C, et al. Design principle and assessing the correlations in Sb-doped  $\text{Ba}_{0.5}\text{Sr}_{0.5}\text{FeO}_{3-\delta}$  perovskite oxide for enhanced oxygen reduction catalytic performance. *J Catal* 2021;395:168-77. DOI
11. Tayyab Z, Rauf S, Xia C, et al. Advanced LT-SOFC based on reconstruction of the energy band structure of the  $\text{LiNi}_{0.8}\text{Co}_{0.15}\text{Al}_{0.05}\text{O}_2 - \text{Sm}_{0.2}\text{Ce}_{0.8}\text{O}_{2-\delta}$  heterostructure for fast ionic transport. *ACS Appl Energy Mater* 2021;4:8922-32. DOI
12. Rauf S, Zhu B, Yousaf Shah MAK, et al. Application of a triple-conducting heterostructure electrolyte of  $\text{Ba}_{0.5}\text{Sr}_{0.5}\text{Co}_{0.1}\text{Fe}_{0.7}\text{Zr}_{0.1}\text{Y}_{0.1}\text{O}_{3-\delta}$  and  $\text{Ca}_{0.04}\text{Ce}_{0.80}\text{Sm}_{0.16}\text{O}_{2-\delta}$  in a high-performance low-temperature solid oxide fuel cell. *ACS Appl Mater Interfaces* 2020;12:35071-80. DOI PubMed
13. Shah MY, Tayyab Z, Rauf S, et al. Interface engineering of bi-layer semiconductor  $\text{SrCoSnO}_{3-\delta}$ - $\text{CeO}_{2-\delta}$  heterojunction electrolyte for boosting the electrochemical performance of low-temperature ceramic fuel cell. *Int J Hydrog Energy* 2021;46:33969-77. DOI

14. Mushtaq N, Lu Y, Xia C, et al. Promoted electrocatalytic activity and ionic transport simultaneously in dual functional  $\text{Ba}_{0.5}\text{Sr}_{0.5}\text{Fe}_{0.8}\text{Sb}_{0.2}\text{O}_{3.8}\text{-Sm}_{0.2}\text{Ce}_{0.8}\text{O}_{2.8}$  heterostructure. *Appl Catal B* 2021;298:120503. DOI
15. Xing Y, Hu E, Wang F, et al. Cubic silicon carbide/zinc oxide heterostructure fuel cells. *Appl Phys Lett* 2020;117:162105. DOI
16. Gao Z, Mogni LV, Miller EC, Railsback JG, Barnett SA. A perspective on low-temperature solid oxide fuel cells. *Energy Environ Sci* 2016;9:1602-44. DOI
17. Zhu B, Raza R, Qin H, Liu Q, Fan L. Fuel cells based on electrolyte and non-electrolyte separators. *Energy Environ Sci* 2011;4:2986. DOI
18. Kudo A, Miseki Y. Heterogeneous photocatalyst materials for water splitting. *Chem Soc Rev* 2009;38:253-78. DOI PubMed
19. Xing Y, Wu Y, Li L, et al. Proton Shuttles in  $\text{CeO}_2/\text{CeO}_{2.8}$  core-shell structure. *ACS Energy Lett* 2019;4:2601-7. DOI
20. Dong W, Tong Y, Zhu B, et al. Semiconductor  $\text{TiO}_2$  thin film as an electrolyte for fuel cells. *J Mater Chem A* 2019;7:16728-34. DOI
21. Agrawal A, Dar TA, Phase DM, Sen P. Type I and type II band alignments in  $\text{ZnO}/\text{MgZnO}$  bilayer films. *Appl Phys Lett* 2014;105:081603. DOI
22. Yousaf Shah MA, Mushtaq N, Rauf S, Xia C, Zhu B. The semiconductor  $\text{SrFe}_{0.2}\text{Ti}_{0.8}\text{O}_{3.8}\text{-ZnO}$  heterostructure electrolyte fuel cells. *Int J Hydrog Energy* 2019;44:30319-27. DOI
23. Chen G, Sun W, Luo Y, et al. Investigation of layered  $\text{Ni}_{0.8}\text{Co}_{0.15}\text{Al}_{0.05}\text{LiO}_2$  in electrode for low-temperature solid oxide fuel cells. *Int J Hydrog Energy* 2018;43:417-25. DOI
24. Chen G, Sun W, Luo Y, et al. Advanced fuel cell based on new nanocrystalline structure  $\text{Gd}_{0.1}\text{Ce}_{0.9}\text{O}_2$  electrolyte. *ACS Appl Mater Interfaces* 2019;11:10642-50. DOI PubMed
25. Rahman A, Harunsani MH, Tan AL, Ahmad N, Hojamberdiev M, Khan MM. Effect of Mg doping on ZnO fabricated using aqueous leaf extract of *Ziziphus mauritiana* Lam. for antioxidant and antibacterial studies. *Bioprocess Biosyst Eng* 2021;44:875-89. DOI PubMed
26. Choudhary MK, Kataria J, Sharma S. Novel green biomimetic approach for preparation of highly stable Au-ZnO heterojunctions with enhanced photocatalytic activity. *ACS Appl Nano Mater* 2018;1:1870-8. DOI
27. Platonov VB, Rumyantseva MN, Frolov AS, Yapyrintsev AD, Gaskov AM. High-temperature resistive gas sensors based on ZnO/SiC nanocomposites. *Beilstein J Nanotechnol* 2019;10:1537-47. DOI PubMed PMC
28. Ievtushenko A, Khyzhun O, Shtepliuk I, Tkach V, Lazorenko V, Lashkarev G. X-ray photoelectron spectroscopy study of nitrogen and aluminum-nitrogen doped ZnO films. *Acta Phys Pol A* 2013;124:858-61. DOI
29. Fan W, Li H, Zhao F, et al. Boosting the photocatalytic performance of (001) BiOI: enhancing donor density and separation efficiency of photogenerated electrons and holes. *Chem Commun* 2016;52:5316-9. DOI PubMed
30. Chang FM, Brahma S, Huang JH, Wu ZZ, Lo KY. Strong correlation between optical properties and mechanism in deficiency of normalized self-assembly ZnO nanorods. *Sci Rep* 2019;9:905. DOI PubMed PMC
31. Mushtaq N, Xia C, Dong W, et al. Tuning the energy band structure at interfaces of the  $\text{SrFe}_{0.75}\text{Ti}_{0.25}\text{O}_{3.8}\text{-Sm}_{0.25}\text{Ce}_{0.75}\text{O}_{2.8}$  heterostructure for fast ionic transport. *ACS Appl Mater Interfaces* 2019;11:38737-45. DOI PubMed
32. Lu Y, Zhu B, Shi J, Yun S. Advanced low-temperature solid oxide fuel cells based on a built-in electric field. *Energy Mater* 2021;1:100007. DOI
33. Zhu B, Mi Y, Xia C, et al. Nano-scale view into solid oxide fuel cell and semiconductor membrane fuel cell: material and technology. *Energy Mater* 2021;1:100002. DOI
34. Zhu B, Wang B, Wang Y, et al. Charge separation and transport in  $\text{La}_{0.6}\text{Sr}_{0.4}\text{Co}_{0.2}\text{Fe}_{0.8}\text{O}_{3.8}$  and ion-doping ceria heterostructure material for new generation fuel cell. *Nano Energy* 2017;37:195-202. DOI
35. Yousaf M, Lu Y, Hu E, et al. Tunable magneto-optical and interfacial defects of Nd and Cr-doped bismuth ferrite nanoparticles for microwave absorber applications. *J Colloid Interface Sci* 2022;608:1868-81. DOI PubMed
36. Song L, Li T, Zhang S. Synthesis and characterization of Ag/AgBrO<sub>3</sub> photocatalyst with high photocatalytic activity. *Mater Chem Phys* 2016;182:119-24. DOI
37. Lacerda LHDS, de Lazaro SR. Isomorphic substitution and intermediary energy levels: a new application of DFT modelling and semiconductor theory to describe p-n type junctions interface in heterostructures: isomorphic substitution in ZnO/BTO. *Phys Status Solidi B* 2017;254:1700119. DOI
38. Catti M, Noel Y, Dovesi R. Full piezoelectric tensors of wurtzite and zinc blende ZnO and ZnS by first-principles calculations. *J Phys Chem Solids* 2003;64:2183-90. DOI
39. Wang Z, Zhang L, Zhang X, et al. Enhanced photocatalytic destruction of pollutants by surface W vacancies in  $\text{V}_w\text{-Bi}_2\text{WO}_6$  under visible light. *J Colloid Interface Sci* 2020;576:385-93. DOI PubMed